Effects of local *p*H on the formation and regulation of cristae morphologies

Dong Hoon Song,[1] Jonghyun Park,[1] Martin A. Philbert,[2] Ann Marie Sastry,[3] and Wei Lu[1,*]
[1]*Department of Mechanical Engineering, University of Michigan, Ann Arbor, Michigan 48109, USA*
[2]*School of Public Health, University of Michigan, Ann Arbor, Michigan 48109, USA*
[3]*Sakti3, Ann Arbor, Michigan, 48108, USA*
(Received 11 April 2014; published 5 August 2014)

Cristae, folded subcompartments of the inner mitochondrial membrane (IMM), have complex and dynamic morphologies. Since cristae are the major site of adenosine triphosphate synthesis, morphological changes of cristae have been studied in relation to functional states of mitochondria. In this sense, investigating the functional and structural significance of cristae may be critical for understanding progressive mitochondrial dysfunction. However, the detailed mechanisms of the formation and regulation of these cristae structures have not been fully elucidated. Among the hypotheses concerning the regulation of cristae morphologies, we exclusively investigate the effects of the local *p*H gradient on the cristae morphologies by using a numerical model. An area-difference induced curvature of the membrane is modeled as a function of local *p*H. This curvature is then applied to the finite element model of a closed lipid bilayer in order to find the energetically favorable membrane configuration. From this study, we substantiate the hypothesis that a tubular crista structure can be formed and regulated by the local *p*H gradient. Through the simulations with various initial conditions, we further demonstrate that the diameter of a crista is mainly determined by the local *p*H gradient, and the energetically favorable direction of crista growth is perpendicular to the longitudinal axis of a mitochondrion. Finally, the simulation results at the mitochondrial scale suggest that the cristae membrane may have a lower local *p*H value and/or a higher cardiolipin composition than the other parts of the IMM.

DOI: 10.1103/PhysRevE.90.022702 PACS number(s): 87.16.Tb, 87.16.A−

I. INTRODUCTION

Mitochondria have been recognized as the primary cellular powerhouses, because their main function is synthesizing adenosine triphosphate (ATP) by oxidative phosphorylation. During oxidative phosphorylation, the electron transport chain pumps protons across the inner mitochondrial membrane (IMM) by using free energy released from a series of redox reactions. The resulting electrochemical gradient of proton is used for synthesizing ATP via ATP synthase [1,2]. These protein complexes involved in ATP synthesis are located in the IMM. In particular, a subcompartment of the IMM called a crista has been considered to be the major site of ATP synthesis since proteins comprising ATP synthase and electron transport chains are more concentrated on cristae membranes [3,4].

The biophysical effects of complex, diverse, and dynamic cristae morphologies have been studied in relation to mitochondrial functions. Folded cristae structures have been speculated as the capacity enhancer for ATP synthesis by providing greater surface area and electrochemical potential [5–7]. Moreover, experimental studies have shown that mitochondria can present distinctive cristae morphologies with respect to their functional and disease states. For example, enlarged cristae were observed in mitochondria with high respiratory activity, while contracted cristae were shown in mitochondria with low respiratory activity [8,9]. Also, loss of cristae structures were observed in neurodegenerative diseases (e.g., Alzheimer's disease, Parkinson's disease, and Huntington's disease) [10,11].

As such, the literature suggests that the cristae morphologies are closely related to mitochondrial functions. Therefore, investigating the biophysical and functional effects of cristae structures may be an instrumental step for understanding progressive mitochondrial dysfunction such as aging and neurodegeneration. Moreover, analyses of the cristae morphologies may help differentiate the multiplicity of known disease and normal states. However, mechanisms of how these cristae structures can be formed and regulated and how this morphology regulation may be related to mitochondrial function have not been fully understood.

To explain the formation and regulation of cristae structures, two hypotheses have been proposed: (i) Cristae morphologies may be related to the distributions of protein complexes [7,12,13], and (ii) cristae morphologies may be regulated by the local *p*H gradient generated from oxidative phosphorylation [14–16]. The first hypothesis is supported by the experimental observation [by using electron microscopy with three-dimensional (3D) image reconstruction] showing long ribbons of ATP synthase dimers located at the apex of cristae membranes [13]. Even though these dimer ribbons may contribute to the formation of cristae structures by bending the membrane, this hypothesis does not provide a sufficient explanation on how the cristae morphologies can be associated with the respiratory activities (or functional states) of mitochondria. The second hypothesis is based on the fact that area per lipid headgroup decreases as *p*H decreases. Thus the local *p*H difference across the membrane can induce the curvature by the area mismatch between two layers of the membrane, and consequently regulate the cristae morphologies. Therefore, in this case, the cristae morphologies can reflect the functional state of a mitochondrion because the local *p*H gradient, which is controlled by respiratory activities, directly represents the functional state and determines the viability of a mitochondrion.

*Corresponding author: weilu@umich.edu

The above hypothesis of the cristae regulation by the local pH gradient was proposed by Khalifat *et al.* [14]. They experimentally showed that the local pH gradient can form a cristaelike invagination on the giant unilamellar vesicle (GUV). The local pH gradient on the GUV was generated by the microinjection of acid. The cardiolipin (CL) containing GUVs presented dynamic and reversible changes of the cristaelike invaginations by acid delivery. They also provided theoretical explanations of observed cristaelike invaginations. Theoretical values of the radii and lengths of cristaelike tubules were calculated and compared with their experimental results. However, this study could not successfully explain why the cristaelike structures have tubular shapes and whether this shape is energetically favorable. Moreover, the mechanism proposed in this study needs to be validated at the mitochondrial scale because of the large size difference between mitochondria and GUVs (i.e., to form a crista at the mitochondrial scale, a much higher local pH gradient may be required because a small crista has a higher curvature than a large crista of similar shape).

However, the experimental validation of this mechanism at the actual mitochondrial scale is restricted by optical resolution and control of the local pH profile. Therefore, simulation models are not only plausible supplements for resolving those experimental limitations, but also excellent techniques for presenting a theoretical understanding of existing observations. For example, a thermodynamic model was used to provide theoretical explanations of experimentally observed cristae morphologies [17–19]. The dynamics of lipid bilayer membranes was modeled and validated with the well-known biological membrane dynamics [20–26]. To date, however, numerical models simulating morphological changes of the IMM associated with the local pH gradient have not been developed.

In this paper, we introduce a model simulating the morphologies of the IMM at the given pH profiles. In Sec. II, an area-difference induced curvature depending on the pH difference across the membrane is modeled. In addition to the estimation of the curvature, the finite element model of lipid bilayer membranes developed by Feng, Ma, and Klug [21,23] is applied to find the energetically favorable membrane configuration. In Sec. III, we present simulation results and investigate (i) how a tubular crista structure can be formed by and disappear due to the local pH gradient, (ii) which factors can affect the cristae membrane morphologies, and (iii) whether the same mechanism proposed by Khalifat *et al.* can be applicable at the mitochondrial scale. Finally, the validity and limitations of this study are discussed.

II. METHODS

Our model system is composed of a closed lipid bilayer with homogeneous composition (the effects of protein compositions are not considered). To reduce the computational cost, we limit our study to two-dimensional (2D) axisymmetric geometries. We first calculate the area-difference induced curvature of the membrane at a given pH difference across the membrane. Finally, to find the membrane configuration having the minimum energy, this curvature is plugged into the lipid bilayer model developed by Feng, Ma, and Klug [21,23].

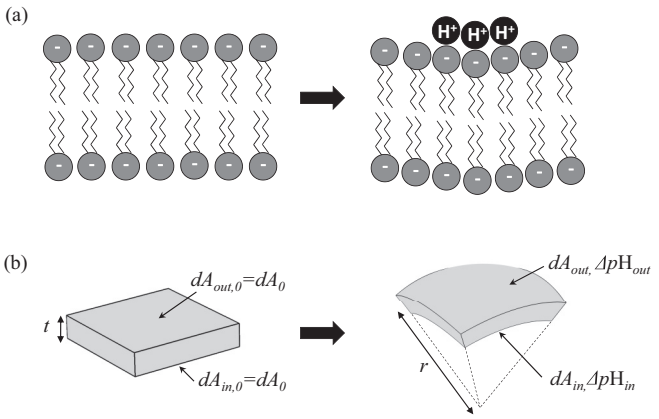

FIG. 1. Curvature of the lipid bilayer induced by local pH. (a) Illustration of a curvature induced by locally introduced protons. (b) Modeling of the pH-dependent area change and resulting area-difference induced curvature.

A. Local pH and curvature of the lipid bilayer

During oxidative phosphorylation, protons are pumped out from the matrix by the electron transport chain and by generating the pH difference across the IMM. This pH difference can induce a curvature by mismatched areas between two layers of the membrane. As illustrated in Fig. 1(a), positively charged protons (or hydrated hydrogen ions) introduced on the outer side of the membrane neutralize the negative charges of lipid headgroups. This electrical neutralization reduces repulsive forces between headgroups and consequently the area per headgroup. This decreased area of the outer layer results in area mismatch between the inner and the outer layer. Finally, the curvature of the lipid bilayer can be induced by this area mismatch.

First, we model the pH-dependent area change similar to thermal expansion by assuming that the area changes linearly with change in pH (this assumption is further discussed in Sec. IV B).

$$A = A_0(1 + \alpha_A \Delta p\mathrm{H}), \tag{1}$$

where A and A_0 are areas of the layer before and after pH change, respectively; α_A is the area expansion coefficient; and ΔpH is the pH difference ($\Delta p\mathrm{H} = p\mathrm{H}–p\mathrm{H}_0$).

From Eq. (1), the infinitesimal areas of the inner and the outer layer after pH change dA_{in} and dA_{out} [see Fig. 1(b)] are

$$dA_{\mathrm{in}} = dA_0(1 + \alpha_A \Delta p\mathrm{H}_{\mathrm{in}}), \tag{2}$$

$$dA_{\mathrm{out}} = dA_0(1 + \alpha_A \Delta p\mathrm{H}_{\mathrm{out}}). \tag{3}$$

On the other hand, dA_{in} and dA_{out} can also be calculated by assuming that the inner and outer layers form concentric spherical surfaces.

$$dA_{\mathrm{in}} = (r - t/2)^2 \sin\theta d\theta d\phi, \tag{4}$$

$$dA_{\mathrm{out}} = (r + t/2)^2 \sin\theta d\theta d\phi, \tag{5}$$

where r is the radius of the midplane of the membrane, t is the thickness of the membrane, θ is a polar angle, and ϕ

is an azimuth angle of a spherical coordinate system. From Eqs. (2)–(5), the area-difference induced curvature of the membrane at the given pH (C_0) is

$$C_0 = \frac{2}{r} = \frac{4(c-1)}{t(c+1)}, \quad \text{where } c = \sqrt{\frac{dA_{\text{out}}}{dA_{\text{in}}}} = \sqrt{\frac{1+\alpha_A \Delta p\text{H}_{\text{out}}}{1+\alpha_A \Delta p\text{H}_{\text{in}}}}. \tag{6}$$

Therefore, C_0 can be determined by the given pH values of the inner and outer surfaces of the membrane. The details of pH profiles used in this simulation will be explained in Sec. II E.

B. Area expansion coefficient (α_A)

The area expansion coefficient (α_A) can be estimated from the measurements of the mean area per lipid molecule at different pH values. For the GUV simulations, we use the mean area per lipid measured in Ref. [14]. The mean area per lipid molecule in monolayers composed of 90 mol % of phosphatidylcholine (PC) and 10 mol % of cardiolipin (CL) was measured at pH 8 and 4. The mean area decreased ~8.6% as pH decreased from 8 to 4. From Eq. (1), this corresponds to α_A of 0.0214. We use this value for the area expansion coefficient of the GUV ($\alpha_{\text{GUV}} = 0.0214$).

For the simulations at the mitochondrial scale, we apply different values of α_A. Since the lipid composition of the IMM is different from that of the GUV, the IMM can have a different α_A. In particular, the IMM has higher CL composition (~20%) [27,28], which is considered to be the main contributor for the pH-dependent area change [14,16,29,30]. Thus, this higher CL composition can provide greater α_A than α_{GUV}. Moreover, it has been speculated that the CL composition in the cristae membrane is even higher [31,32]. However, more work needs to be done in estimating accurate CL composition in the cristae membrane. Therefore, we perform simulations with various α_A in the range between α_{GUV} and $10\alpha_{\text{GUV}}$.

C. Lipid bilayer model

To simulate the lipid bilayer mechanics, we employed the model developed by Feng, Ma, and Klug [21,23]. We modify the model suitable for the 2D axisymmetric geometry and large deformation. Since the lipid bilayer mechanics is not a main focus of this study, we will briefly explain the lipid bilayer model (see Ref. [23] for more detailed descriptions of the lipid bilayer model).

Following Ref. [23], the total energy functional of the membrane I can be written as

$$I = \Pi + I^{\text{con}} + I^{\text{reg}}, \tag{7}$$

where Π is the potential energy, I^{con} is the constraint energy, and I^{reg} is the regularization energy. The potential energy (Π) is constructed from the Helfrich functional [33–35].

$$\Pi = \int \frac{1}{2} K(2H - C_0)^2 A ds, \tag{8}$$

where K is the bending modulus, H is the mean curvature, C_0 is the area-difference induced curvature, and Ads is the infinitesimal surface area element. The potential energy is only composed of the bending energy because we assume no work is done by external forces. The Gaussian curvature term in the Helfrich functional is neglected by the Gauss-Bonnet theorem; if we assume no topological change (i.e., fixed Euler characteristic) during membrane deformation, the integral of the Gaussian curvature over the closed membrane surface remains constant. To enforce area and volume constraints, the constraint energy (I^{con}) is established by applying the augmented Lagrangian approach.

$$I^{\text{con}} = \frac{\mu_V}{2}(V - V_0)^2 - p_n V + \frac{\mu_A}{2}(A - A_0)^2 + \alpha_n A, \tag{9}$$

where V and V_0 are the enclosed volumes of the current configuration and the initial shape, respectively. A and A_0 are the surface areas of the current configuration and the initial shape, respectively (a detailed description of the initial shape is provided in Sec. II E). μ_V and μ_A are penalty parameters for the volume and area constraints, respectively. p_n and α_n are Lagrange multiplier estimates for the volume and area constraints at the nth iteration, respectively. By employing both penalty terms and Lagrange multiplier estimates in Eq. (9), the augmented Lagrangian approach can enforce the volume and surface area constraints without having very large penalty parameters. However, the constraint energy (I^{con}) can only impose global constraints. This constraint does not penalize in-plane deformations of finite element nodes and does not enforce local incompressibility. Especially in large deformation problems, these in-plane deformations may induce degenerate modes. To resolve this problem, we use dashpot regularization energy (which penalizes in-plane deformations) introduced by Ma and Klug [23].

$$I^{\text{reg}} = \sum_{\text{edge } ab} \frac{k}{2}(l_{ab} - L_{ab})^2, \tag{10}$$

where k is a spring constant, l_{ab} and L_{ab} are lengths between nodes a and b of current and reference configurations, respectively.

From the principle of minimum potential energy, the weak form of the energy functional is derived from the variation of a functional.

$$\delta I = \delta\Pi + \delta I^{\text{con}} + \delta I^{\text{reg}}, \tag{11}$$

$$\delta\Pi = \int \left[K(2H - C_0)\delta(2H)A + \frac{1}{2}K(2H - C_0)^2 \delta A \right] ds, \tag{12}$$

$$\delta I^{\text{con}} = \int [-p_{n+1}\delta V + \alpha_{n+1}\delta A] ds, \tag{13}$$

$$\delta I^{\text{reg}} = \sum_{\text{edge } ab} k(l_{ab} - L_{ab})\delta l_{ab}, \tag{14}$$

where $p_{n+1} = p_n - \mu_V(V - V_0)$ and $\alpha_{n+1} = \alpha_n + \mu_A(A - A_0)$. (The derivations of δH, δA, and δV in a 2D axisymmetric coordinate system can be found in Appendix A.) This weak

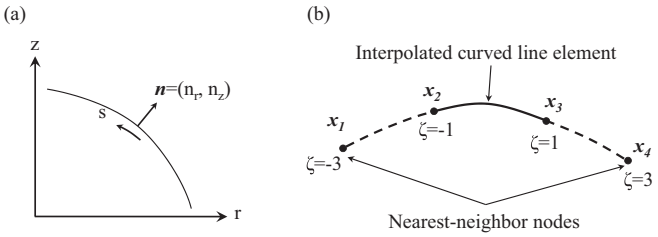

FIG. 2. 2D axisymmetric coordinate system and geometry of the surface represented by curved line elements. (a) The membrane surface is parametrized by curvilinear coordinates: $\boldsymbol{x} = \boldsymbol{x}(s)$. (b) A curved line element is obtained from interpolating four node points including nearest-neighbor nodes.

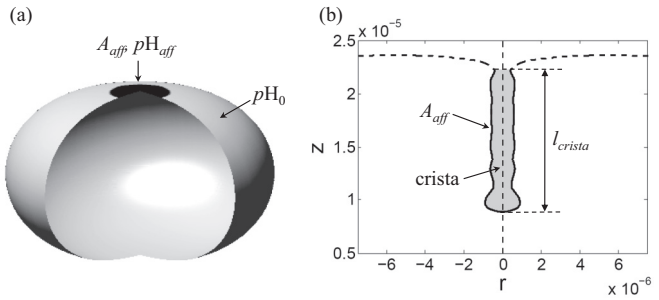

FIG. 3. pH profile on the membrane surface and morphological parameters of a cristaelike structure. (a) The area affected by acid delivery (A_{aff}) is set on the top center part of the membrane. (b) Morphological parameters are calculated from the shaded area (enclosed by the affected area).

form of the energy functional is used to find the conjugate direction for the numerical optimization method.

D. Finite element approximation and energy minimization

Curved line elements are used to approximate the membrane surface in the 2D axisymmetric coordinate system. Because a curvature calculation requires the second derivative of a function, the interpolation (or shape) function needs to be at least a quadratic polynomial in order to have a nonzero curvature. To implement this, we use a cubic polynomial function as a shape function. As can be seen in Fig. 2(b), shape functions are obtained from interpolating four node points including nearest-neighbor nodes.

$$\boldsymbol{x}(\zeta) = \sum_{i=1}^{4} N_i(\zeta)\boldsymbol{x_i}, \tag{15}$$

where $\boldsymbol{x}$ is a position vector of the membrane surface, N_i is a shape function, and $\boldsymbol{x_i}$ is a node-point vector (see Appendix B for more details). The total energy functional and its weak form are discretized by substituting the position vector $\boldsymbol{x}$ with a node-point vector $\boldsymbol{x_i}$. At the given node positions, the numerical values of these discretized equations [Eqs. (7) and (11)] can be evaluated by using a three-point Gaussian quadrature. Finally, simulations are performed by applying the nonlinear conjugate gradient method. The nonlinear conjugate method is used to find the local minimum of the total energy functional without deriving the stiffness matrix. The weak form of the total energy functional is used to find the steepest descent direction and the conjugate direction for the numerical optimization. In this study, we use the Polak-Ribière-Polyak formula for calculating the conjugate gradient update parameter [36,37].

E. Initial configurations, pH profiles, and postprocessing

We use oblate and prolate spheroids as initial shapes because the simulations are performed in 2D axisymmetric geometries. These initial shapes are parametrized by the equivalent radius (R_0) and the reduced volume (v).

$$R_0 = \sqrt{A/4\pi}, \tag{16}$$

$$v = \frac{V}{(4\pi/3)R_0^3}. \tag{17}$$

Since these initial shapes are not in equilibrium, the equilibrium shapes of these initial shapes are obtained by performing simulations with zero area-difference induced curvature. Finally, these equilibrium shapes are used as the initial configurations.

To simulate the experimental conditions described in Ref. [14], we define the area affected by acid delivery (A_{aff}). As can be seen in Fig. 3(a), we set the affected area on the top center part of the membrane surface. To study the effects of the affected area, we change the percentage of the affected area (P_{aff}).

$$P_{\text{aff}} = \frac{A_{\text{aff}}}{A_0}. \tag{18}$$

We assign pH values at the node points of the affected area ($p\text{H}_{\text{aff}}$), while pH values elsewhere are assumed to remain at 8 ($p\text{H}_0$). For numerical integration, pH values at the Gauss points are linearly interpolated from the nodal values. We decrease pH values of the affected area from $p\text{H}_0$ with a decrement of 0.1. However, during this process, the affected area can change due to the updates of node points. This problem is resolved by repositioning the node points. After every energy minimization step, the node points are repositioned along the surface of the membrane in order to have the same affected area. The overall simulation procedure is summarized as follows:

(i) Set initial parameters and the reference configuration $\boldsymbol{X}$.

(ii) Solve for the current configuration $\boldsymbol{x}$ at the given pH profile by the total energy minimization.

(iii) Reposition the node points.

(iv) Update the reference configuration: $\boldsymbol{X} = \boldsymbol{x}$.

(v) Update parameters (μ_V, μ_A, p_n, and α_n).

(vi) Repeat steps (ii)–(v) until $|v - v_0|/v_0 < 10^{-5}$ and $I^{\text{reg}}/I < 10^{-5}$.

After solving for the configuration at each pH step, the morphology of a cristaelike structure is quantified. Figure 3(b) shows an example of a cristaelike structure. To quantify this morphology, we calculate a length (l_{crista}), a radius (r_{crista}), an aspect ratio (R_A), and a surface-to-volume ratio (R_{SV}) of the

cristaelike structure.

$$r_{\text{crista}} = \sqrt{\frac{-\int_{\text{crista}} \pi r^2 z' ds}{\pi l_{\text{crista}}}}, \tag{19}$$

$$R_A = \frac{l_{\text{crista}}}{2r_{\text{crista}}}, \tag{20}$$

$$R_{SV} = \frac{\int_{\text{crista}} 2\pi r (r'^2 + z'^2)^{1/2} ds}{-\int_{\text{crista}} \pi r^2 z' ds}. \tag{21}$$

[Note: a radius (r_{crista}) of a crista was defined as a radius of an equivalent cylinder.] Finally, we analyze the simulation results with these morphological parameters.

III. RESULTS

We first simulate the morphological change of the membrane at the GUV scale ($R_0 = 30$ μm). The formation and disappearance of the cristaelike structure with respect to the pH values on the affected area ($p\text{H}_{\text{aff}}$) is studied. We also investigate the factors which may affect the morphology of the cristaelike structure and examine which morphological parameters may represent functional states of mitochondria. Finally, simulations are performed at the mitochondrial scale ($R_0 = 1$ μm). At this smaller scale, we examine the conditions required for the tubular cristae formation.

A. Formation and disappearance of the cristaelike structure at the GUV scale

The morphological change of the membrane is studied at the GUV scale. We use an oblate spheroid with $v = 0.95$ and $R_0 = 30$ μm as an initial shape and the area expansion coefficient (α_A) of 0.0214 (α_{GUV}).

First, the equilibrium shape of the membrane is simulated at pH 8 (zero area-difference induced curvature). We assign the affected area at the top center of the membrane surface as described in Sec. II E. The percentage of the affected area over the total surface area (P_{aff}) is maintained at 0.5%. We decrease the pH value of the affected area ($p\text{H}_{\text{aff}}$) from 8 to 7 with a decrement of 0.1. As can be seen in Fig. 4, the affected area starts to form a concave geometry due to the negative area-difference induced curvature. As $p\text{H}_{\text{aff}}$ decreases, a single spherical shape of a cristaelike structure emerges at $p\text{H}_{\text{aff}} = 7.6$. Then the affected area evolves to a structure of connected spheres (or nearly spherical shapes) with smaller radii. This structure of connected spheres may not be a configuration that globally minimizes the potential energy. Instead, it may be a selected configuration, which locally minimizes the potential energy, among multistable configurations. At the given area-difference induced curvature, a radius of a sphere minimizing the bending energy is larger than that of a tubule or a cylinder (i.e., because one of the principal curvatures of a cylinder is zero, the other needs to be two times greater than that of a sphere in order to have the same mean curvature). Thus the structure of connected spheres requires less deformation and emerges as an intermediate configuration before finally forming a tubular cristaelike structure. This cristaelike structure formation process (including intermediate configurations) is consistent with those observed in the GUV experiment [14]. Moreover, in the presence of mechanical anisotropy (or misfit strains), shape transitions among multistable morphologies (e.g., flat shell, helical ribbon, saddle shape, and cylindrical configuration) have been found in many other physical and biological systems [38–40].

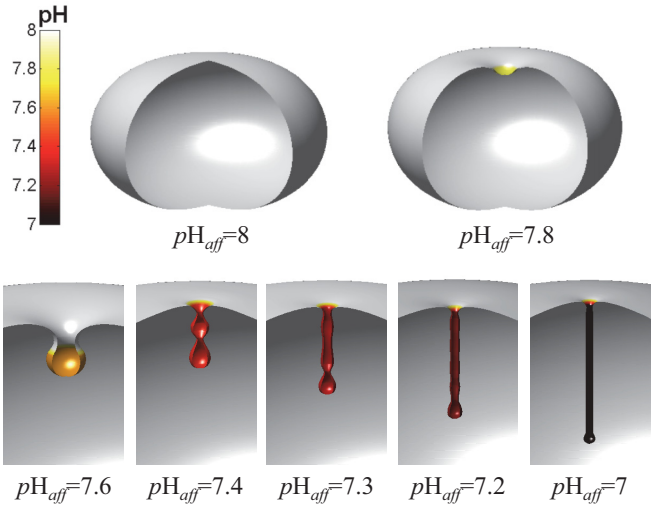

FIG. 4. (Color online) Formation process of the cristaelike structure at selected $p\text{H}_{\text{aff}}$. An oblate spheroid with $v = 0.95$ and $R_0 = 30$ μm is used as an initial shape. α_A of 0.0214 (α_{GUV}) and P_{aff} of 0.5% are used

To study the reversibility of this membrane deformation, we increase $p\text{H}_{\text{aff}}$ from 7 to 8 with an increment of 0.1. The membrane configuration at $p\text{H}_{\text{aff}} = 7$ in Fig. 4 is used as an initial configuration for this simulation. Figure 5 shows the disappearance of the cristaelike structure with increasing $p\text{H}_{\text{aff}}$. At the same $p\text{H}_{\text{aff}}$, the morphologies of the cristaelike structure shown during the disappearance process (Fig. 5) are very similar to those shown during the formation process (Fig. 4). Even though our numerical methods search for a local minimum, the optimized membrane configuration at the given pH profile is minimally affected by the initial condition or path. Therefore, cristae morphologies may be good indicators

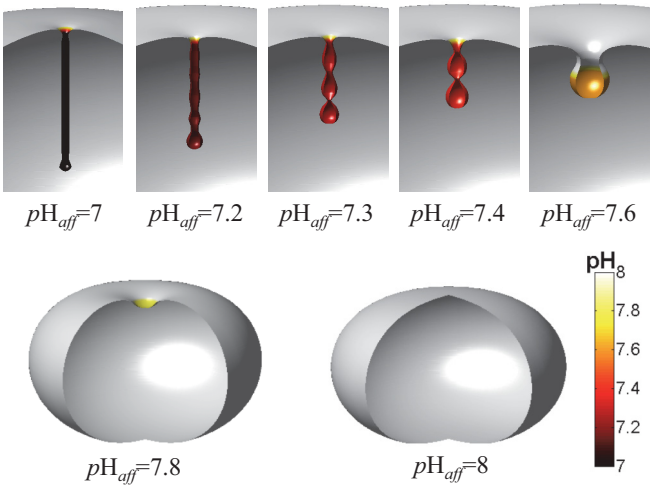

FIG. 5. (Color online) Disappearance process of the cristaelike structure at selected $p\text{H}_{\text{aff}}$. The membrane configuration at $p\text{H}_{\text{aff}} = 7$ in Fig. 4 is used as an initial configuration. α_A of 0.0214 (α_{GUV}) and P_{aff} of 0.5% were used.

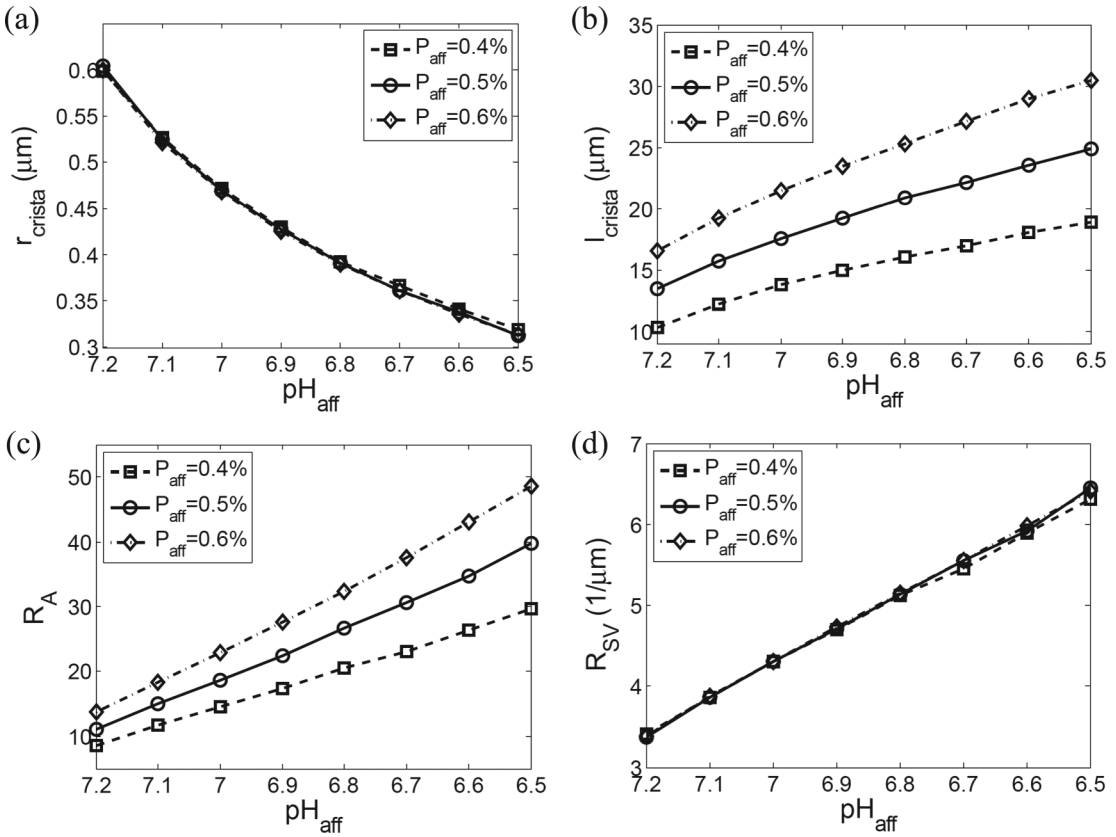

FIG. 6. The effects of the percentage of the affected area (P_{aff}) on the morphological parameters of a cristaelike structure. (a) Change in the radius of a cristaelike structure. (b) Change in the length of a cristaelike structure. (c) Change in the aspect ratio of a cristaelike structure. (d) Change in the surface-to-volume ratio of a cristaelike structure.

of local pH, which is typically difficult to directly measure due to limitations in experiments. Finally, the cristaelike structure is completely removed and the membrane is fully recovered to the original configuration when the local pH gradient disappears ($p\text{H}_{\text{aff}} = 8$). Therefore, if a mitochondrion loses its pH gradient across the membrane, it can also lose its cristae structures as observed in a dysfunctional mitochondrion [10,11].

B. The effects of P_{aff} and initial shapes

To investigate the factors determining the morphology of the cristaelike structure, membrane models with different P_{aff} and initial shapes are simulated. The morphology of the cristaelike structure at each $p\text{H}_{\text{aff}}$ is analyzed by using four morphological parameters described in Sec. II E: r_{crista}, l_{crista}, R_A, and R_{SV}.

The morphological changes of the cristaelike structures with three different P_{aff} (0.4%, 0.5%, and 0.6%) are analyzed. The same initial configuration (oblate spheroid with $v = 0.95$ and $R_0 = 30$ μm) and the area expansion coefficient (α_A) of 0.0214 are used. As can be seen in Figs. 6(b) and (6c), the cristaelike structure developed from a larger affected area is longer and consequently has a higher aspect ratio. On the other hand, the percentage of the affected area does not show significant effects on both r_{crista} and R_{SV} [Fig. 6(a) and (6d)]. Because these two morphological parameters are mainly determined by the area-difference induced curvature (which is directly related to the local pH), they are only associated with $p\text{H}_{\text{aff}}$. Thus, r_{crista} and R_{SV} may be key morphological parameters reflecting the functional states of mitochondria.

To study the effects of the initial shape, four different initial configurations are simulated at the same conditions ($R_0 = 30$ μm, $\alpha_A = 0.0214$, $P_{\text{aff}} = 0.5\%$). Figure 7 shows the effects of the initial shapes on the morphological parameters. Oblate spheroids with two different reduced volumes ($v = 0.95$ and 0.85) exhibit almost identical morphological parameters over the entire range of $p\text{H}_{\text{aff}}$, whereas prolate spheroids show delayed growth of tubular cristaelike structures. In the case of the oblate spheroid, the initial pH value for tubular cristaelike structure formation is 7.2. The prolate spheroids with $v = 0.95$ and $v = 0.85$ start to form a tubular cristaelike structure at pH 7.1 and 7, respectively. Moreover, the prolate spheroids develop initially thicker and shorter cristaelike structures. This delayed formation and development of the cristaelike structure from the prolate spheroids may be contributed from the higher positive mean curvature of the affected area (i.e., the membrane invagination may be hindered by the more convex affected area of prolate spheroids). However, after the cristaelike structures are fully formed, the morphological parameters of prolate spheroids are converged to those of oblate spheroids.

C. Cristae formation at the mitochondrial scale

The morphological change of the membrane is finally simulated at the mitochondrial scale. We investigate whether

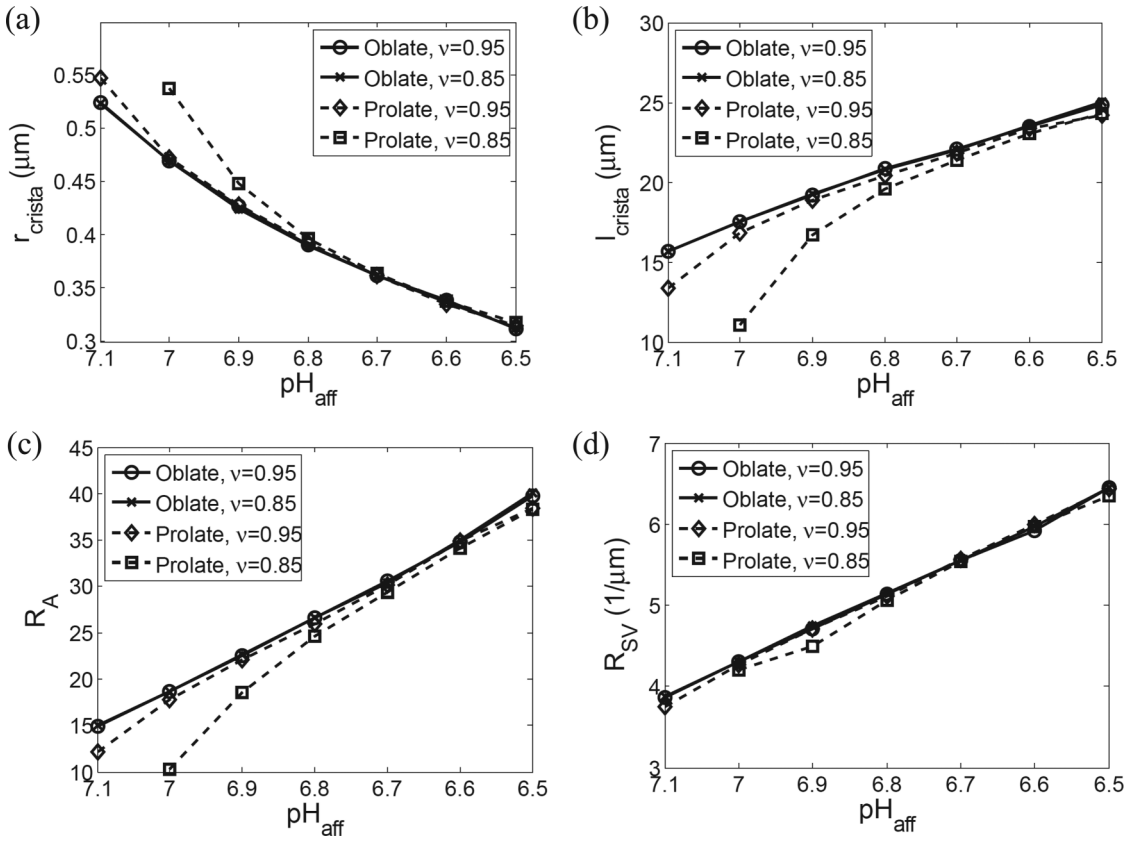

FIG. 7. The effects of the initial shape on the morphological parameters of a cristaelike structure. Oblate and prolate spheroids with $\nu = 0.95$ and 0.85 are used as initial shapes. (a) Change in the radius of a cristaelike structure. (b) Change in the length of a cristaelike structure. (c) Change in the aspect ratio of a cristaelike structure. (d) Change in the surface-to-volume ratio of a cristaelike structure.

the same mechanism applied at the GUV scale can still be valid at the smaller mitochondrial scale. An oblate spheroid with $\nu = 0.95$ and $R_0 = 1$ μm is used as an initial shape. We maintain the percentage of the affected area (P_{aff}) of 0.5%, while $p\text{H}_{\text{aff}}$ is decreased from 8 to 4.

As can be seen in Fig. 8(a), when α_A of 0.0214 (α_{GUV}) is applied, the affected area forms a concave geometry instead of a tubular cristaelike structure. This is due to the higher negative area-difference induced curvature required to form a smaller crista.

The higher negative area-difference induced curvature can be achieved by a higher local pH gradient (lower $p\text{H}_{\text{aff}}$) or a greater α_A. Since the applicable range of $p\text{H}_{\text{aff}}$ is limited (a $p\text{H}_{\text{aff}}$ lower than 4 might not be feasible due to the lipid degradation in acid), we perform simulations with greater area expansion coefficients (α_A is increased up to 10 times α_{GUV}). When $\alpha_A = 5\alpha_{\text{GUV}}$, a tubular cristaelike structure is fully developed at $p\text{H}_{\text{aff}} = 4$ [Fig. 8(b)].

We further investigate a critical pH value ($p\text{H}_{\text{crit}}$) required to form a tubular cristaelike structure. From the simulation results, we calculate the $p\text{H}_{\text{crit}}$ where the membrane forms a crista with a diameter ($2r_{\text{crista}}$) of 40 nm. Figure 8(c) shows the $p\text{H}_{\text{crit}}$ with different α_A. To form a tubular crista at pH 5 and 6, α_A of the cristae membrane should be greater than 6.4 times and 9.5 times α_{GUV}, respectively. As explained in Sec. II B, for the actual cristae membrane, this much greater α_A may be achieved by a much higher CL composition of the cristae membrane. However, the accurate CL composition and the area expansion coefficient of the cristae membrane are still unknown.

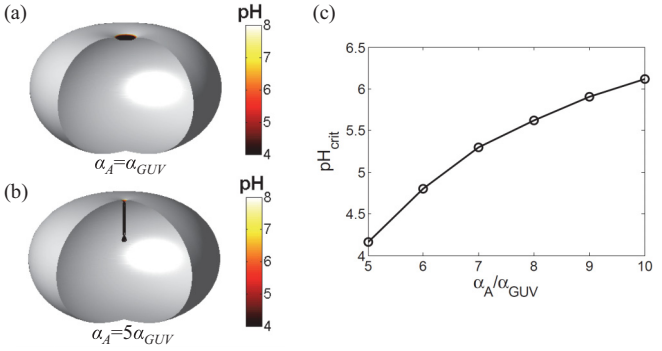

FIG. 8. (Color online) Cristae formation at the mitochondrial scale. (a) The membrane morphology simulated with α_{GUV} at $p\text{H}_{\text{aff}} = 4$. (b) The membrane morphology simulated with $5\alpha_{\text{GUV}}$ at $p\text{H}_{\text{aff}} = 4$. (c) Critical pH values required to form tubular cristae with different area expansion coefficients.

IV. DISCUSSION

In this section, by comparing the existing experimental observations, we first discuss the validity of the major findings in this study. In addition to the validation, the limitations from the model assumptions and simplifications are discussed.

A. Comparison with existing experimental observations

Through the simulation model, we showed that a tubular cristae structure can be formed and regulated by the local *p*H gradient. Even though the model did not reproduce complex and entangled geometries (due to the application of simple axisymmetric geometries), early steps of the cristaelike structure formation and final steps of the disappearance (from a tubular structure to connected spheres, a single sphere, and a concave geometry) were consistent with those observed in Ref. [14]. This morphological change was more clearly seen during the disappearance of a cristaelike structure (see figures in Ref. [14]). This might be due to the fact that the complete disappearance of the local *p*H gradient after removing acid delivery takes more time than the development of the local *p*H gradient, and this slower process can provide more time for having a fully equilibrated membrane configuration similar to those simulated by the energy minimization method. Furthermore, the simulation results, which showed a decrease in the tubular crista radius accompanied by an increase in the local *p*H gradient, correspond to the experimental observations of actual distinctive cristae structures: swollen cristae were observed in mitochondria at state 3 (low local *p*H gradient), while narrow tubular cristae were shown in mitochondria at state 4 (high local *p*H gradient) [8].

Additionally, we investigated the effects of the affected area and the initial shape. First, the simulation results suggested that the affected area can only change the length, but not the diameter of a crista. From these simulation results, we can infer that the diameter of each crista may be nearly uniform, if the local *p*H values on the cristae membranes are comparable. This inference is supported by the observations that found relatively small variations in tubular cristae diameters (20–40 nm) [41,42]. Second, we showed that the initial shape can affect the growth of a tubular crista: The initial tubular cristae formation on the membrane with higher positive mean curvature requires more local *p*H gradient. Thus the tubular cristae formation on a flat or concave surface is more favorable. This finding explains the direction of tubular cristae that is mostly perpendicular to the longitudinal axis of a mitochondrion [41,43].

Simulations at the mitochondrial scale were performed with a range of area expansion coefficients. At this small scale, developing a tubular crista requires a greater area expansion coefficient and higher local *p*H gradient. In reality, the area expansion coefficient of the cristae membrane may be much greater than that estimated from the GUV due to higher CL composition. Additionally, the higher local *p*H gradient can be obtained by the locally concentrated protons on the cristae membrane (proton trapping by its concave geometry and higher CL composition) [14,16,29,30]. According to our simulation results, the local CL composition and *p*H gradient on the cristae membrane might be higher than those speculated in the existing literature. However, due to the limitations in optical resolution and diffusion, these local values have not been accurately measured.

B. Model assumptions and limitations

We discuss the limitations from the model assumptions and simplifications. As mentioned earlier, we limited our study to the 2D axisymmetric coordinate system in order to reduce the computational cost and avoid numerical instabilities by applying extremely fine elements. Because of the symmetric geometries and *p*H profiles, detailed membrane morphologies that deviated from symmetric conditions could not be simulated.

In addition, we did not consider the effects of *p*H on mechanical properties of the membrane, such as the area expansion coefficient (α_A) and the bending modulus (K). However, studies have found that these mechanical properties can be altered by *p*H [44–46].

Figure 9(a) shows the *p*H-dependent area changes estimated from the GUV experiment [14] and the molecular dynamics (MD) simulation [45]. The MD simulation results show that the area expansion coefficient does not depend considerably on *p*H (i.e., almost linear relationship between the mean area per headgroup and *p*H). In the GUV experiment, however, the functional form of the correlation between the area per headgroup and *p*H cannot be determined because the mean area per headgroup was measured only at two different *p*H values (*p*H 4 and 8). Since the compositions of lipid used in

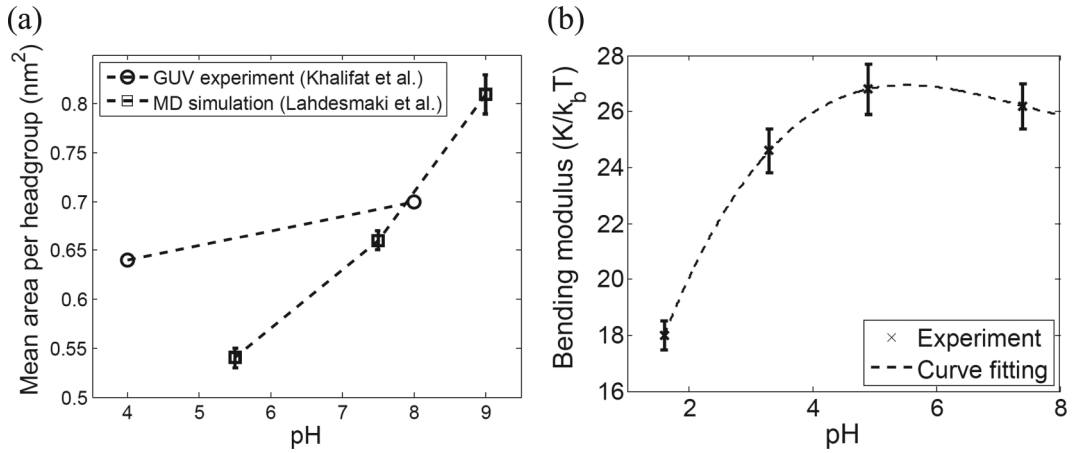

FIG. 9. The effects of *p*H on the mechanical properties of lipid bilayers. (a) The correlation between the mean area per headgroup and *p*H estimated from the GUV experiment and the molecular dynamics (MD) simulation. (b) Bending modulus as a function of *p*H.

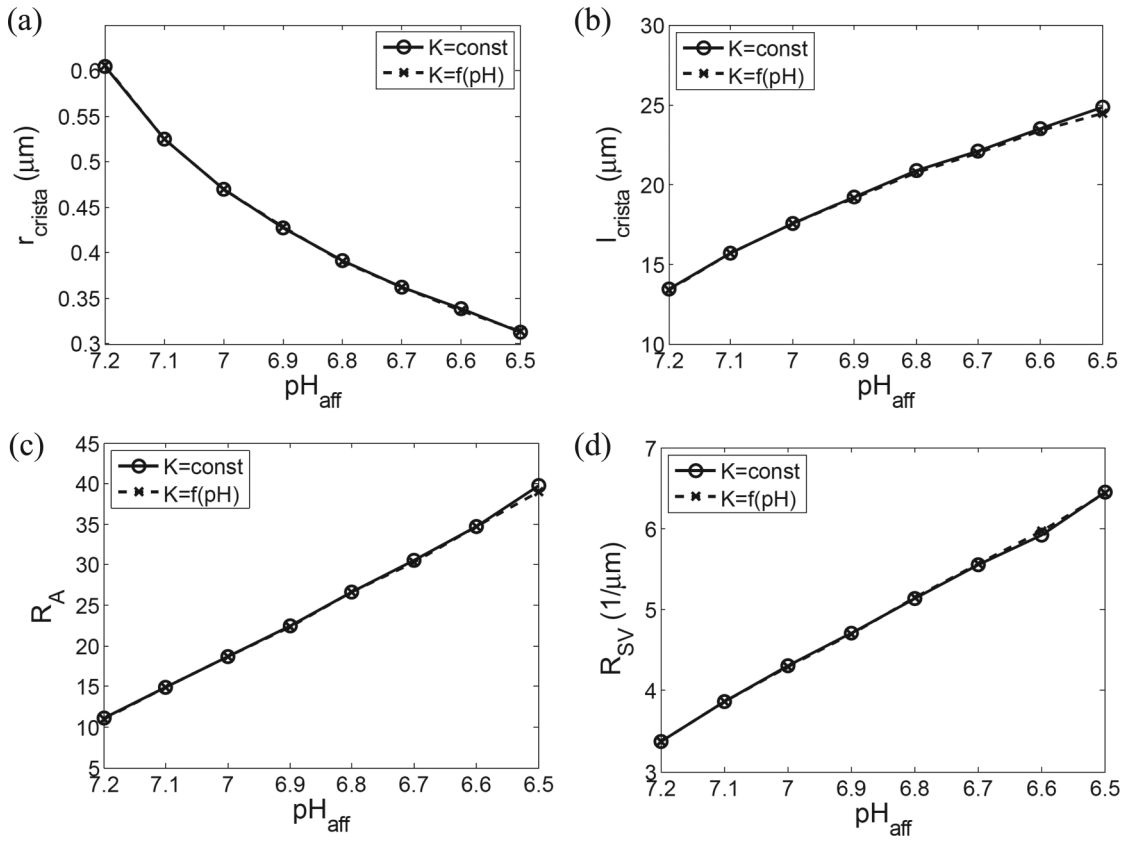

FIG. 10. The effects of the pH-dependent bending modulus on the morphological parameters of a cristaelike structure (oblate spheroid with $v = 0.95$, $R_0 = 30\ \mu$m, $\alpha_A = \alpha_{\mathrm{GUV}}$, $P_{\mathrm{aff}} = 0.5\%$).

the MD simulation and the GUV experiment are different, the validity of our assumption of the linear relationship between the area per headgroup and pH is not yet conclusive.

As can be seen in Fig. 9(b), the bending modulus may be a function of pH. In order to examine whether the pH-dependent bending modulus may affect the simulation results, we model the bending modulus as a function of pH [$K = f(p\mathrm{H})$, where f is a cubic polynomial function] by curve fitting the experimental data in Ref. [44]. This bending modulus is then applied to our simulation model. Within the range of pH values used in this study (from pH 6.5 to 8), applying the pH-dependent bending modulus does not notably affect our simulation results (Fig. 10). Thus, the bending modulus of the IMM may be assumed as a constant (pH independent) within the feasible pH range of mitochondria.

Next, with an assumption of a homogeneous lipid membrane, the effects of protein complexes were not modeled. However, the insertion of a protein complex such as ATP synthase has been hypothesized to bend the membrane [12,13]. Thus, in conjunction with the local pH gradient, the spontaneous curvature of the protein complex may contribute to the formation and regulation of cristae structures.

Finally, we assumed localized protons on the cristae membrane (or the affected area by acid delivery) without modeling the diffusion of protons along the membrane surface. Even though the meticulous modeling of the pH profile may provide more precise cristae dynamics, it requires consideration of many modeling parameters and physics (such as activities of proton source and sink, electric potential, and transport of proton), which may complicate the effects of the local pH on cristae morphologies.

V. CONCLUSIONS

The complex and widely varied cristae morphologies have been studied in relation to mitochondrial functions. However, the mechanisms of how these cristae structures can be regulated and are related to energetic functions of mitochondria are not clear. To date, the formation and regulation of cristae morphologies have been hypothesized (i) by the distributions of protein complexes and (ii) by the local pH gradient. Among these two hypotheses, we exclusively investigated the effects of the local pH gradient by using a numerical model.

To develop a numerical model simulating the morphologies of the IMM at the given pH profiles, we first modeled an area-difference induced curvature induced by the pH difference across the membrane. This curvature was then applied to the finite element model of a closed lipid bilayer in order to find the energetically favorable membrane configuration.

From this study, we developed a numerical model simulating the morphological changes of cristae structures from which we substantiated the hypothesis that tubular cristae structures can be formed and regulated by the local pH gradient and investigated the effects of the local pH gradient on the morphological parameters of the cristae structures. Moreover, through the simulations with various initial conditions, we provided the potential explanations of the relatively uniform diameter and direction of the tubular cristae (experimentally

observed from mitochondria in the orthodox configuration): the diameter of a crista is mainly determined by the local pH gradient, and the energetically favorable direction of a crista is perpendicular to the longitudinal axis of a mitochondrion (the initial formation of a crista on a less convex membrane surface requires less pH gradient). Finally, we presented that the formation of the tubular cristae structure at the actual mitochondrial scale requires a greater area expansion coefficient (even in high local pH gradient) than that estimated from the GUV experiment. This simulation result supports the hypothesis that the cristae membrane may have a higher composition of CL than the other parts of the IMM.

ACKNOWLEDGMENTS

This work was supported by National Institutes of Health Grant No. 1R01 ES08846.

APPENDIX A: VARIATION OF THE MEAN CURVATURE, SURFACE AREA, AND ENCLOSED VOLUME

As can be seen in Fig. 2(a), the normal vector $\boldsymbol{n}$ is

$$\boldsymbol{n} = (n_r, n_z) = \left[\frac{z'}{(r'^2+z'^2)^{1/2}}, \frac{-r'}{(r'^2+z'^2)^{1/2}}\right], \tag{A1}$$

where the prime ($'$) denotes a partial differentiation with respect to the parameter s.

From the definition of the mean curvature and Eq. (A1), the mean curvature can be derived as

$$\begin{aligned} 2H = \nabla\cdot\boldsymbol{n} &= \frac{1}{r}\frac{\partial(rn_r)}{\partial r} + \frac{\partial n_z}{\partial z} \\ &= \frac{r'z'' - z'r''}{(r'^2+z'^2)^{3/2}} + \frac{z'}{r(r'^2+z'^2)^{1/2}}. \end{aligned} \tag{A2}$$

By the first variation of Eq. (A2), δH can be obtained as

$$\delta(2H) = c_1\delta r + c_2\delta r' + c_3\delta r'' + c_4\delta z' + c_5\delta z'', \tag{A3}$$

where $c_1 = -\frac{z'}{r^2(r'^2+z'^2)^{1/2}}$, $c_2 = \frac{z'^2z''-2r'^2z''+3r'r''z'-(r'z'^3+r'^3z')/r}{(r'^2+z'^2)^{5/2}}$, $c_3 = -\frac{z'}{(r'^2+z'^2)^{3/2}}$, $c_4 = \frac{-r'^2r''-3r'z'z''+2r''z'^2+(r'^4+r'^2z'^2)/r}{(r'^2+z'^2)^{5/2}}$, and $c_5 = \frac{r'}{(r'^2+z'^2)^{3/2}}$.

The total surface area can be calculated as

$$A_{\text{tot}} = \int A\,ds = \int 2\pi r(r'^2+z'^2)^{1/2}ds.$$

From the above equation, the infinitesimal surface area is

$$A = 2\pi r(r'^2+z'^2)^{1/2}. \tag{A4}$$

Then, the first variation of A is

$$\begin{aligned} \delta A = 2\pi[&(r'^2+z'^2)^{1/2}\delta r + rr'(r'^2+z'^2)^{-1/2}\delta r' \\ &+ rz'(r'^2+z'^2)^{-1/2}\delta z']. \end{aligned} \tag{A5}$$

Similarly,

$$V_{\text{tot}} = \int V\,ds = \int \pi r^2 z'\,ds, \quad V = \pi r^2 z', \tag{A6}$$

$$\delta V = (2\pi r z')\delta r + (\pi r^2)\delta z'. \tag{A7}$$

APPENDIX B: FINITE ELEMENT SHAPE FUNCTION

A finite element shape function is obtained from interpolating four node points. As can be seen in Fig. 2(b), these four node points are two end points of the element and two nearest-neighbor nodes. To construct isoparametric shape functions, the following conditions are applied.

$$\begin{array}{llll} N_1(-3)=1, & N_1(-1)=0, & N_1(1)=0, & N_1(3)=0, \\ N_2(-3)=0, & N_2(-1)=1, & N_2(1)=0, & N_2(3)=0, \\ N_3(-3)=0, & N_3(-1)=0, & N_3(1)=1, & N_3(3)=0, \\ N_4(-3)=0, & N_4(-1)=0, & N_4(1)=0, & N_4(3)=1. \end{array}$$

Because there are four conditions for each equation, we use cubic polynomial functions.

From the above conditions, the resulting shape functions are

$$N_1 = \tfrac{1}{48}(-x^3+3x^2+x-3), \tag{B1}$$

$$N_2 = \tfrac{1}{48}(3x^3-3x^2-27x+27), \tag{B2}$$

$$N_3 = \tfrac{1}{48}(-3x^3-3x^2+27x+27), \tag{B3}$$

$$N_4 = \tfrac{1}{48}(x^3+3x^2-x-3). \tag{B4}$$

APPENDIX C: MODEL VERIFICATION

For the model verification, we simulate the equilibrium shapes of the membranes with different initial shapes and zero local pH gradient (i.e., zero area-difference induced curvature). The normalized potential energy ($\Pi/8\pi K$) calculated from the equilibrium shape is compared with the result obtained from Seifert *et al.* [47]. Figure 11 shows the normalized potential energy and equilibrium shapes of oblate and prolate spheroids with different reduced volume. As can be seen in this figure, our simulation results are in good agreement with those from Seifert *et al.*

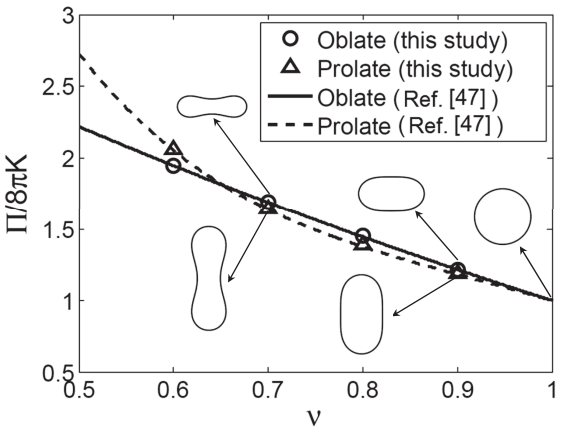

FIG. 11. Comparison of the normalized potential energy calculated in this study with those obtained from Ref. [47]. Equilibrium shapes of oblate and prolate spheroids at selected reduced volumes are presented in the inset.

[1] P. Mitchell, Biol. Rev. Cambridge Philos. Soc. **41**, 445 (1966).
[2] N. Kocherginsky, Prog. Biophys. Mol. Biol. **99**, 20 (2009).
[3] R. W. Gilkerson, J. M. L. Selker, and R. A. Capaldi, FEBS Lett. **546**, 355 (2003).
[4] F. Vogel, C. Bornhövd, W. Neupert, and A. S. Reichert, J. Cell Biol. **175**, 237 (2006).
[5] C. A. Mannella, D. R. Pfeiffer, P. C. Bradshaw, I. I. Moraru, B. Slepchenko, L. M. Loew, C. E. Hsieh, K. Buttle, and M. Marko, IUBMB Life **52**, 93 (2001).
[6] G. Perkins, E. Bossy-Wetzel, and M. H. Ellisman, Exp. Neurol. **218**, 183 (2009).
[7] M. Zick, R. Rabl, and A. S. Reichert, Biochim. Biophys. Acta, Mol. Cell Res. **1793**, 5 (2009).
[8] C. A. Mannella, Biochim. Biophys. Acta, Mol. Cell Res. **1763**, 542 (2006).
[9] G. A. Perkins and M. H. Ellisman, J. Struct. Biol. **173**, 117 (2011).
[10] S. K. Sharma, J. Neurocytol. **32**, 329 (2003).
[11] Z. X. Yu, J. Neurosci. **23**, 2193 (2003).
[12] M.-F. Giraud, P. Paumard, V. Soubannier, J. Vaillier, G. Arselin, B. Salin, J. Schaeffer, D. Brèthes, J.-P. di Rago, and J. Velours, Biochim. Biophys. Acta, Bioenerg. **1555**, 174 (2002).
[13] M. Strauss, G. Hofhaus, R. R. Schroder, and W. Kuhlbrandt, EMBO J **27**, 1154 (2008).
[14] N. Khalifat, N. Puff, S. Bonneau, J.-B. Fournier, and M. I. Angelova, Biophys. J. **95**, 4924 (2008).
[15] J. B. Fournier, N. Khalifat, N. Puff, and M. I. Angelova, Phys. Rev. Lett. **102**, 018102 (2009).
[16] N. Khalifat, J.-B. Fournier, M. I. Angelova, and N. Puff, Biochim. Biophys. Acta Biomembranes **1808**, 2724 (2011).
[17] C. Renken, G. Siragusa, G. Perkins, L. Washington, J. Nulton, P. Salamon, and T. G. Frey, J. Struct. Biol. **138**, 137 (2002).
[18] A. Ponnuswamy, J. Nulton, J. M. Mahaffy, P. Salamon, T. G. Frey, and A. R. C. Baljon, Phys. Biol. **2**, 73 (2005).
[19] M. Ghochani, J. D. Nulton, P. Salamon, T. G. Frey, A. Rabinovitch, and A. R. C. Baljon, Biophys. J. **99**, 3244 (2010).
[20] T. Taniguchi, Phys. Rev. Lett. **76**, 4444 (1996).
[21] F. Feng and W. S. Klug, J. Comput. Phys. **220**, 394 (2006).
[22] J. Demongeot, N. Glade, O. Hansen, and A. Moreira, Biochimie **89**, 1049 (2007).
[23] L. Ma and W. S. Klug, J. Comput. Phys. **227**, 5816 (2008).
[24] C. M. Funkhouser, F. J. Solis, and K. Thornton, Soft Matter **6**, 3462 (2010).
[25] K. Guo and J. Li, J. Phys.: Condens. Matter **23**, 285103 (2011).
[26] M. Rahimi and M. Arroyo, Phys. Rev. E **86**, 011932 (2012).
[27] R. Hovius, H. Lambrechts, K. Nicolay, and B. de Kruijff, Biochim. Biophys. Acta, Biomembr. **1021**, 217 (1990).
[28] G. Daum and J. E. Vance, Prog. Lipid Res. **36**, 103 (1997).
[29] M. Schlame, D. Rua, and M. L. Greenberg, Prog. Lipid Res. **39**, 257 (2000).
[30] M. Schlame and M. Ren, Biochim. Biophys. Acta, Biomembr. **1788**, 2080 (2009).
[31] M. Bogdanov, E. Mileykovskaya, and W. Dowhan, in *Lipids in Health and Disease*, edited by P. Quinn and X. Wang (Springer, Netherlands, 2008), p. 197.
[32] E. Mileykovskaya and W. Dowhan, Biochim. Biophys. Acta, Biomembr. **1788**, 2084 (2009).
[33] P. B. Canham, J. Theor. Biol. **26**, 61 (1970).
[34] W. Helfrich, Z. Naturforsch. C **28**, 693 (1973).
[35] E. A. Evans, Biophys. J. **14**, 923 (1974).
[36] B. T. Polyak, USSR Comput. Math. Math. Phys. **9**, 94 (1969).
[37] J. Gilbert and J. Nocedal, SIAM J. Optim. **2**, 21 (1992).
[38] S. Armon, E. Efrati, R. Kupferman, and E. Sharon, Science **333**, 1726 (2011).
[39] Z. Chen, Q. Guo, C. Majidi, W. Chen, D. J. Srolovitz, and M. P. Haataja, Phys. Rev. Lett. **109**, 114302 (2012).
[40] Q. Guo, A. K. Mehta, M. A. Grover, W. Chen, D. G. Lynn, and Z. Chen, Appl. Phys. Lett. **104**, 211901 (2014).
[41] G. Perkins, C. Renken, M. E. Martone, S. J. Young, M. Ellisman, and T. Frey, J. Struct. Biol. **119**, 260 (1997).
[42] G. A. Perkins, C. W. Renken, T. G. Frey, and M. H. Ellisman, J. Neurosci. Res. **66**, 857 (2001).
[43] R. Schmidt, C. A. Wurm, A. Punge, A. Egner, S. Jakobs, and S. W. Hell, Nano Lett. **9**, 2508 (2009).
[44] M. B. Boggara, A. Faraone, and R. Krishnamoorti, J. Phys. Chem. B **114**, 8061 (2010).
[45] K. Lähdesmäki, O. Ollila, A. Koivuniemi, P. T. Kovanen, and M. T. Hyvönen, Biochim. Biophys. Acta, Biomembr. **1798**, 938 (2010).
[46] Y. Zhou and R. M. Raphael, Biophys. J. **92**, 2451 (2007).
[47] U. Seifert, K. Berndl, and R. Lipowsky, Phys. Rev. A **44**, 1182 (1991).